

## Synthesis and characterization of $\text{CuFe}_2\text{O}_4/\text{CeO}_2$ nanocomposites

R. Kalai Selvan<sup>a,b,\*</sup>, C.O. Augustin<sup>a</sup>, V. Šepelák<sup>c,1</sup>, L. John Berchmans<sup>a</sup>,  
C. Sanjeeviraja<sup>b</sup>, A. Gedanken<sup>d</sup>

<sup>a</sup> Electroprometallurgy Division, Central Electrochemical Research Institute, Karaikudi 630006, India

<sup>b</sup> Department of Physics, Alagappa University, Karaikudi 630003, India

<sup>c</sup> Institute of Physical and Theoretical Chemistry, Braunschweig University of Technology, Hans-Sommer-Strasse 10,  
D-38106 Braunschweig, Germany

<sup>d</sup> Department of Chemistry and Kanbar Laboratory for Nanomaterials, Center for Advanced Materials and Nanotechnology,  
Bar-Ilan University, Ramat Gan 52900, Israel

### ARTICLE INFO

#### Article history:

Received 24 December 2007

Received in revised form 10 May 2008

Accepted 27 May 2008

#### Keywords:

Spinel ferrite

Nanocomposite

Electrical properties

Mossbauer spectra

### ABSTRACT

$\text{CuFe}_2\text{O}_4/x\text{CeO}_2$  ( $x = 0, 1, 5, 10$  and  $20$  wt%) nanocomposites have been prepared by urea–nitrate combustion method. The particle size of the as-prepared  $\text{CuFe}_2\text{O}_4/5$  wt%  $\text{CeO}_2$  nanocomposite is  $5$ – $10$  nm which has been revealed from TEM and HRTEM images. The as-synthesized materials have been sintered at four different temperatures ( $600, 800, 1000$  and  $1100$  °C) for  $5$  h. The XRD analysis of the samples reveals that the prepared materials possess tetragonal structure and have the composite behaviour. The  $1100$  °C sintered samples have further been characterized by FT-IR, UV–vis, SEM, ac electrical conductivity, dielectric constant, loss tangent, and Mössbauer spectra. The SEM images clearly show that  $\text{CeO}_2$  grows on the surface of the  $\text{CuFe}_2\text{O}_4$ . The electrical properties enumerate the ferrimagnetic behaviour of the synthesized materials. The Mössbauer spectra confirm both the inverse spinel structure of the prepared materials and the  $\text{Fe}^{3+}$  state of iron ions.

© 2008 Elsevier B.V. All rights reserved.

### 1. Introduction

Synthesis and characterization of nanocomposites have gained prominent interest in recent years due to their tailor-made properties. The term nanocomposite encompasses a variety of distinctly different materials mixed at the nanometric scale with specific applications. Some of the reported types of nanocomposites are magnetic–metal ( $\text{Fe}_3\text{O}_4$ –Au) [1], magnetic–metallic oxide (Zn, Ni Ferrite–NiO) [2], magnetic–polymer ( $\text{CoFe}_2\text{O}_4$ –Polypyrrolle) [3], magnetic–semiconductors ( $\text{Fe}_3\text{O}_4$ –PbS) [4], magnetic–alloy ( $(\text{Ni}_{0.5}\text{Zn}_{0.5})\text{Fe}_2\text{O}_4$ – $\text{FeNi}_3$ ) [5], magnetic–zeolite [6], etc. The present study deals with the spinel structure ( $\text{CuFe}_2\text{O}_4$ ) made as composite with the layered fluorite-type structure ( $\text{CeO}_2$ ) and its characterization. In particular,  $\text{CuFe}_2\text{O}_4$  has unique characteristics when compared with other metallic ferrites because of its Jahn–Teller ( $\text{Cu}^{2+}$ ) ions. The ideal  $\text{CuFe}_2\text{O}_4$  is known to be an inverse spinel, where  $\text{Cu}^{2+}$  ions occupy octahedral [B] sites and  $\text{Fe}^{3+}$  ions occupy both tetrahedral (A) and octahedral sites. However, it is

widely known that the cation distribution in  $\text{CuFe}_2\text{O}_4$  is a complex function of processing parameters and depends on the preparation method of the material.

Very recently, spinel type ferrites such as  $\text{CoFe}_2\text{O}_4$  [7,8],  $\text{NiFe}_2\text{O}_4$  [9,10],  $\text{ZnFe}_2\text{O}_4$  [11], and  $\text{CaFe}_2\text{O}_4$  [12] have gained a prominent interest in the field of energy storage devices especially negative electrodes in Li-ion batteries. In this regard, we have recently reported on  $\text{CuFe}_2\text{O}_4/\text{SnO}_2$  nanocomposite [13] as a potential alternative anode for Li-ion batteries. Subsequently, here we have prepared  $\text{CuFe}_2\text{O}_4/\text{CeO}_2$  nanocomposite and characterized the structural, electrical and magnetic properties of the materials. The EXAFS and XANES studies of  $\text{CuFe}_2\text{O}_4/x\text{CeO}_2$  ( $x = 0, 5, 20$  wt%) nanocomposites have been reported elsewhere [14].  $\text{CeO}_2$  is supposed to be one of the most favorable candidate for the anode material [15,16] in Li-ion batteries when compared with other metal oxides of  $\text{SnO}_2$  [17],  $\text{TiO}_2$  [18],  $\text{Fe}_2\text{O}_3$  [19] and  $\text{NiO}$  [20] due to its unique properties such as large oxygen storage capacity, high thermal stability, facile electrical conductivity, diffusivity and the variable valency of  $\text{Ce}^{3+}$  and  $\text{Ce}^{4+}$  [16]. Similarly, the surface modification [21] is an important phenomenon in Li-ion batteries leading to an enhancement of the electrochemical activity of the electrodes. Among the surface-modified functional oxide materials [22,23],  $\text{CeO}_2$  has gained enormous interest due to an enhancement of the electrochemical stability of the positive electrodes including  $\text{LiMn}_2\text{O}_4$  [24],  $\text{LiCoO}_2$  [25] and  $\text{LiNi}_{0.8}\text{Co}_{0.2}\text{O}_2$  [26].

\* Corresponding author.

E-mail address: [selvankram@rediffmail.com](mailto:selvankram@rediffmail.com) (R.K. Selvan).

<sup>1</sup> On leave from the Slovak Academy of Sciences, Watsonova 45, SK-04353 Košice, Slovakia.

**Table 1**  
The quantity of the reactants for the synthesis of  $\text{CuFe}_2\text{O}_4/x\text{CeO}_2$  nanocomposites (for 100 g) and the yields

Sample	Reactants (g)				Yields (%)
	Cu $(\text{NO}_3)_2 \cdot 6\text{H}_2\text{O}$	Fe $(\text{NO}_3)_3 \cdot 9\text{H}_2\text{O}$	Ce $(\text{NO}_3)_3 \cdot 6\text{H}_2\text{O}$	CO $(\text{NH}_2)_2$	
$\text{CuFe}_2\text{O}_4/1 \text{ wt}\% \text{ CeO}_2$	99.00	332.60	2.52	158.74	88.00
$\text{CuFe}_2\text{O}_4/5 \text{ wt}\% \text{ CeO}_2$	95.00	319.29	12.60	153.74	85.00
$\text{CuFe}_2\text{O}_4/10 \text{ wt}\% \text{ CeO}_2$	90.00	302.00	25.20	147.85	85.00
$\text{CuFe}_2\text{O}_4/20 \text{ wt}\% \text{ CeO}_2$	80.00	268.00	50.54	134.97	87.00

Hence, considering the importance of the surface modified nanocomposites, a detailed preliminary study has been carried out on nanocrystalline  $\text{CuFe}_2\text{O}_4$  with  $\text{CeO}_2$  at four different concentrations of 1, 5, 10, 20 wt% prepared by simple combustion method. The structural (XRD, FT-IR, UV-vis spectra), morphological (SEM, TEM, HRTEM, SAED), electrical (ac electrical conductivity, dielectric constant, loss tangent) and magnetic (Mössbauer spectra) properties of the material have also been investigated and reported herein.

## 2. Experimental

The  $\text{CuFe}_2\text{O}_4/x \text{ wt}\% \text{ CeO}_2$  ( $x=0, 1, 5, 10, 20$ ) nanocomposites were prepared using urea-nitrate combustion method [27]. The stoichiometric quantities of starting materials, viz.,  $\text{Cu}(\text{NO}_3)_2 \cdot 6\text{H}_2\text{O}$ ,  $\text{Fe}(\text{NO}_3)_3 \cdot 9\text{H}_2\text{O}$ ,  $\text{Ce}(\text{NO}_3)_3$  and  $\text{CO}(\text{NH}_2)_2$  were dissolved in 100 ml distilled water. The actual quantities of the reactants for the preparation of each nanocomposite (for 100 g) and the yields are given in Table 1. The mixed nitrate-urea solution was heated at  $110^\circ\text{C}$ , with continuous stirring. After the evaporation of excess of water, a highly viscous gel, known as precursor, has been obtained. Subsequently, the gel was ignited at  $300^\circ\text{C}$  to evolve the undesirable gaseous products, which has resulted in the formation of desired product in the form of foamy powder. The presented (Table 1) yields are not exactly correct. Due to the combustion reaction, lot of products are coming out the reaction vessel. So we cannot calculate the exact value. Subsequently, the powder was sintered at different temperatures (600, 800, 1000 and  $1100^\circ\text{C}$ ) for 5 h to obtain ultrafine powders of  $\text{CuFe}_2\text{O}_4/\text{CeO}_2$  nanocomposites.

The compound formation, phase purity and crystallinity of the ferrite materials were identified by powder X-ray diffraction (XRD) technique using an X-ray diffractometer (PANalytical (Make), X'pert PRO (Model), Cu  $K\alpha$  radiation;  $\lambda_{\text{Cu}} = 1.5405 \text{ \AA}$ ). The FT-IR spectra of the samples were recorded with the KBr discs in the range of  $400\text{--}1000 \text{ cm}^{-1}$  using a PerkinElmer spectrophotometer (PerkinElmer, UK, Paragon-500 model). Diffuse reflectance spectroscopy measurements were carried out on a Cary Varian 1E spectrometer in the range of  $200\text{--}800 \text{ nm}$ . The particle size was analyzed using TEM (JEOL-JEM 100SX microscope) operating at an accelerating voltage of  $200 \text{ kV}$ . The morphological features have been analyzed through SEM (JEOL S-3000 Model). The ac conductivity measurements were made at room temperature using impedance analyzer HIOKI 3532 in the frequency range of  $42 \text{ Hz}$  to  $5 \text{ MHz}$ . The room-temperature Mössbauer measurements were made in transmission geometry using a conventional spectrometer in a constant acceleration mode. A  $^{57}\text{Co}/\text{Rh}$   $\gamma$ -ray source was used. The velocity scale was calibrated relative to  $^{57}\text{Fe}$  in Rh. A proportional counter was used to detect the transmitted  $\gamma$ -rays. Mössbauer spectral analysis software RECOIL [28] was used for the quantitative evaluation of the spectra. The degree of inversion ( $\lambda$ ) was calculated from the Mössbauer subspectral areas ( $I_{\text{A}}/I_{\text{B}} = (f_{\text{A}}/f_{\text{B}})\lambda/(2-\lambda)$ ) assuming that the ratio of the recoilless fractions is  $f_{\text{A}}/f_{\text{B}} = 1$ . Here, the degree of inversion is defined as a fraction of the tetrahedral (A) sites occupied by iron cations; i.e., the structural formula of copper ferrite may be written as  $(\text{Cu}_{1-\lambda}\text{Fe}_\lambda)(\text{Cu}_\lambda\text{Fe}_{2-\lambda})\text{O}_4$ , where round and square brackets denote sites of tetrahedral (A) and octahedral [B] coordination, respectively.

## 3. Results and discussion

### 3.1. Structural studies

The XRD patterns of as-prepared  $\text{CuFe}_2\text{O}_4/x \text{ wt}\% \text{ CeO}_2$  nanocomposites and thermally treated at different temperatures (600, 800, 1000 and  $1100^\circ\text{C}$ ) are shown in Fig. 1. The as-prepared (Fig. 1a) sample contains broad diffraction peaks corresponding to  $\text{CuFe}_2\text{O}_4$  along with the presence of  $\text{CuO}$  and  $\text{Fe}_2\text{O}_3$  phases. The observed broad peaks indicate the nanocrystalline nature of the as-synthesized materials as well as the amorphous behaviour of the materials. When the sintering temperature increases to  $600^\circ\text{C}$ , large number of peaks emerged that correspond to impurity phases

of precursor. In order to avoid the impurity phases, the samples were further sintered at  $800^\circ\text{C}$ . As expected, the XRD pattern reveals the formation of only  $\text{CuFe}_2\text{O}_4$  compound with the lattice planes of (202), (220), (310), (311), (222), (400), (004), etc. [14]. Samples sintered at higher temperatures of 1000 and  $1100^\circ\text{C}$  exhibit very sharp and well-defined peaks confirming the increased crystallinity of the compounds. Unfortunately, no peak for  $\text{CeO}_2$  is identified, which infers that the added  $\text{CeO}_2$  is dissolved in the spinel structure of  $\text{CuFe}_2\text{O}_4$  [23] or otherwise it coated on the surface of the  $\text{CuFe}_2\text{O}_4$  particles [22]. Generally, the Bragg planes of (422) and (440) correspond to tetrahedral and octahedral sites of spinel type materials, respectively [29]. For  $\text{CuFe}_2\text{O}_4/1 \text{ wt}\% \text{ CeO}_2$  sample, the relative intensity of the XRD peak corresponding to the (440) plane,  $I_{440}$ , increases from 6.82 to 9.47 compared with the parent  $\text{CuFe}_2\text{O}_4$  [28]. This indicates that the added  $\text{Ce}^{4+}$  ions enter into the octahedral [B] sites causing the replacement of some of the  $\text{Fe}^{3+}$  ions from [B]-sites into (A)-sites. As a consequence, the relative intensity of the XRD peak corresponding to the (422) plane  $I_{422}$ , increases from 6.51 to 8.14. Thus, it can be concluded that the added  $\text{Ce}^{4+}$  ions enter into the B-sites of copper ferrite. The calculated lattice constant values (Table 2) enumerate that the samples possess tetragonal structure and the values slightly increase with the addition of  $\text{CeO}_2$ , which may be due to the difference in ionic radii of  $\text{Ce}^{4+}$  and  $\text{Fe}^{3+}$  ( $r(\text{Ce}^{4+}) = 0.87 \text{ \AA}$ ,  $r(\text{Fe}^{3+}) = 0.645 \text{ \AA}$ ). The primary particle size calculated using Debye-Scherrer formula (Table 2) indicates the growth of particles with increasing temperature.

The XRD patterns of  $\text{CuFe}_2\text{O}_4/5, 10$  and  $20 \text{ wt}\% \text{ CeO}_2$  nanocomposites sintered at different temperatures are shown in Fig. 1b,c and d. It is observed that the intensity of  $\text{CeO}_2$  peaks, i.e., (111) at  $28^\circ$  and (311) at  $56.7^\circ$ , in all the samples increases with increase in  $\text{CeO}_2$  wt% as well as with sintering temperature. A scrutiny of the lattice parameter values of  $c$  and  $a$  makes it clear the retention of tetragonal structure all along. It is understood that the tetragonal structure of parent  $\text{CuFe}_2\text{O}_4$  remains more or less intact. Thus, addition of  $\text{CeO}_2$  does not have much influence on the original structure of  $\text{CuFe}_2\text{O}_4$ , and hence it is presumed that a composite has been resulted. The calculated primary particle size of the materials decreases with increasing concentration of  $\text{CeO}_2$  (see Table 2), which is due to the formation of secondary phases that hinders the grain growth of the primary particles [30].

FT-IR spectra of  $1100^\circ\text{C}$  sintered  $\text{CuFe}_2\text{O}_4/x\text{CeO}_2$  ( $x=0, 1, 5, 10, 20 \text{ wt}\%$ ) nanocomposites are shown in Fig. 2. In ferrite the metal cations are situated in two different sub-lattices namely tetrahedral (A-sites) and octahedral (B-sites) according to the geometric configuration of the oxygen ion nearest neighbours. The band  $\nu_1$  around  $600 \text{ cm}^{-1}$  is attributed to stretching vibration of tetrahedral complexes and  $\nu_2$  around  $400 \text{ cm}^{-1}$  to that of octahedral complexes. It can be seen that the observed band at  $570 \text{ cm}^{-1}$  in the spectrum of  $\text{CuFe}_2\text{O}_4$  is attributed to the stretching vibration of tetrahedrally coordinated  $\text{Fe}^{3+}\text{--O}^{2-}$  bonds. The similar spectral features are also observed for all composites irrespective of the amount of added  $\text{CeO}_2$ . At higher concentration of  $\text{CeO}_2$  ( $\geq 10 \text{ wt}\%$ ), a small band is noticed around  $650 \text{ cm}^{-1}$ , which is due to the Ce-O vibration [31].

Fig. 3 shows the UV-vis spectra of  $\text{CuFe}_2\text{O}_4$  sample and of  $\text{CuFe}_2\text{O}_4/x\text{CeO}_2$  ( $x=0, 1, 5, 10, 20 \text{ wt}\%$ ) nanocomposites sintered at

1100 °C. The optical band gap ( $E_g$ ) values are calculated from the spectra using the following relation:  $(\alpha E)^2 = \text{const} (E - E_g)$ , where  $\alpha$  is the absorption coefficient,  $E$  is the photon energy;  $E_g$  values can be derived by extrapolating the linear portion of the  $(\alpha E)^2$  vs.  $E_g$  plot. The  $\alpha$  and  $E$  can be converted from the absorbance,  $A$ , using the relationship  $\alpha = (A \times \ln 10)/d$  and  $E = 1240/\lambda_p$ , respectively, where  $d$  is the thickness of the material and  $\lambda_p$  is the wavelength [32]. The optical band gap values obtained are 2.63, 2.68, 2.54, 2.53, and

2.46 eV for  $\text{CuFe}_2\text{O}_4/x\text{CeO}_2$  ( $x=0, 1, 5, 10, \text{ and } 20$  wt%), respectively, which shows that the materials have semiconducting behaviour.

### 3.2. Morphological studies

Fig. 4 shows the SEM images of  $\text{CuFe}_2\text{O}_4/x\text{CeO}_2$  ( $x=1, 5$  and 20 wt%) nanocomposites sintered at 1100 °C. Smooth and well-defined grains with grain boundaries are observed in

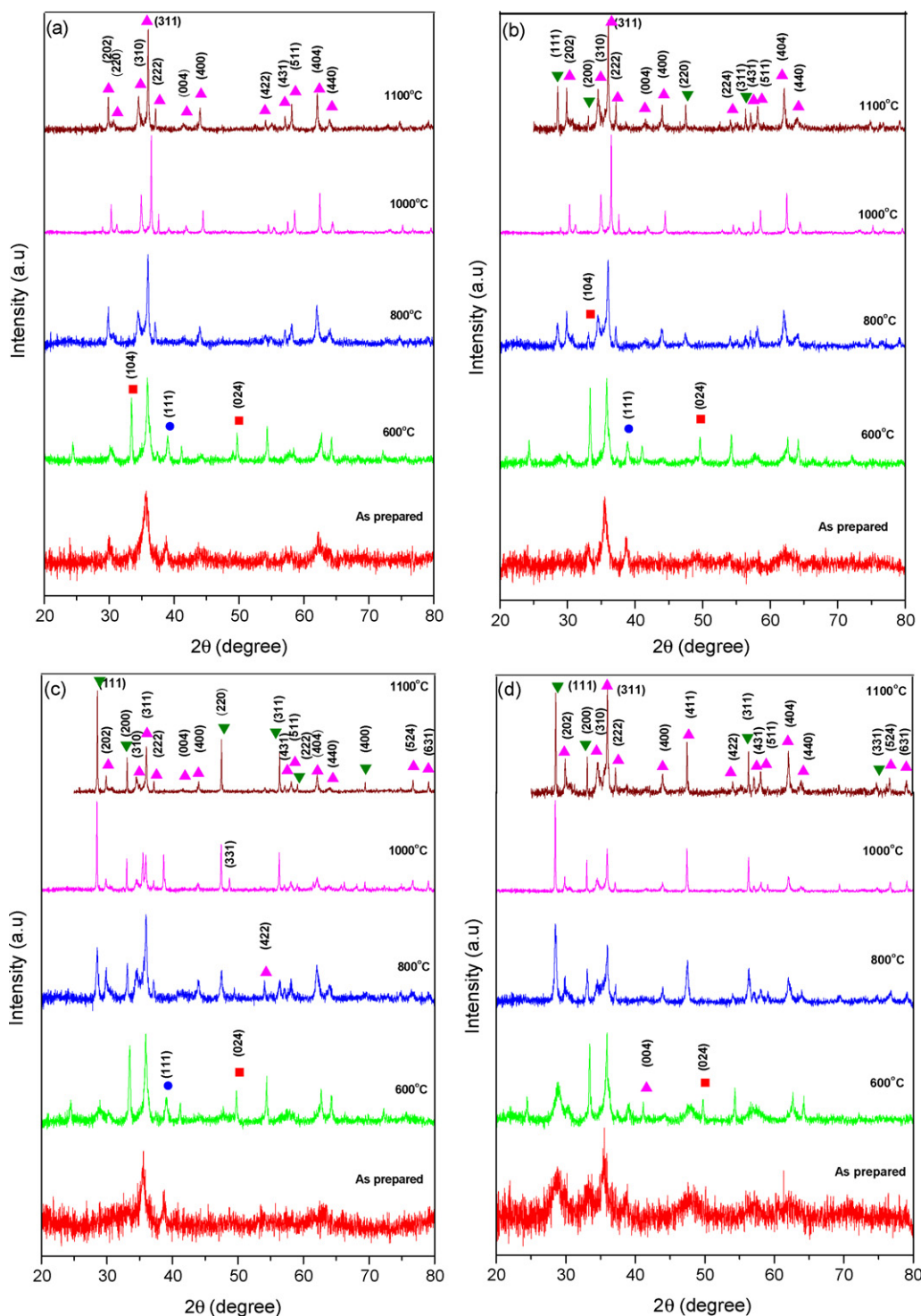


**Fig. 1.** XRD patterns of  $\text{CuFe}_2\text{O}_4/1$  wt%  $\text{CeO}_2$  (a),  $\text{CuFe}_2\text{O}_4/5$  wt%  $\text{CeO}_2$  (b),  $\text{CuFe}_2\text{O}_4/10$  wt%  $\text{CeO}_2$  (c),  $\text{CuFe}_2\text{O}_4/20$  wt%  $\text{CeO}_2$  (d) nanocomposites; (▲)  $\text{CuFe}_2\text{O}_4$ , (●)  $\text{CuO}$ , (■)  $\text{Fe}_2\text{O}_3$ , (▼)  $\text{CeO}_2$ .

**Table 2**  
XRD parameters (lattice constants  $a$  and  $c$ , and grain size  $D$ ) of the  $\text{CuFe}_2\text{O}_4/x\text{CeO}_2$  nanocomposites

Sample	Parameters	Sintered at °C				
		Green	600	800	1000	1100
$\text{CuFe}_2\text{O}_4/1 \text{ wt}\% \text{ CeO}_2$	$a(\text{\AA})$	8.3546	8.2778	8.2667	8.1612	8.2613
	$c(\text{\AA})$	–	8.4784	8.6577	8.5113	8.6566
	$c/a$	–	1.024	1.047	1.042	1.005
	$D(\text{nm})$	$12 \pm 3.4$	$18 \pm 4.6$	$25 \pm 4.9$	$32 \pm 4.2$	$49 \pm 6.2$
$\text{CuFe}_2\text{O}_4/5 \text{ wt}\% \text{ CeO}_2$	$a(\text{\AA})$	8.3726	8.3099	8.2646	8.2076	8.2582
	$c(\text{\AA})$	–	8.3783	8.6561	8.5708	8.6481
	$c/a$	–	1.008	1.0473	1.044	1.047
	$D(\text{nm})$	$8 \pm 4.9$	$15 \pm 4.7$	$21 \pm 2.6$	$28 \pm 5.6$	$41 \pm 7.1$
$\text{CuFe}_2\text{O}_4/10 \text{ wt}\% \text{ CeO}_2$	$a(\text{\AA})$	8.3986	8.2854	8.2775	8.2789	8.2631
	$c(\text{\AA})$	–	8.3636	8.6373	8.6442	8.6459
	$c/a$	–	1.009	1.043	1.044	1.046
	$D(\text{nm})$	$5 \pm 2.2$	$10 \pm 4.5$	$16 \pm 3.9$	$25 \pm 4.2$	$37 \pm 6.6$
$\text{CuFe}_2\text{O}_4/20 \text{ wt}\% \text{ CeO}_2$	$a(\text{\AA})$	8.3657	8.2833	8.2672	8.2767	8.2607
	$c(\text{\AA})$	–	8.3401	8.6555	8.6647	8.6521
	$c/a$	–	1.006	1.046	1.046	1.047
	$D(\text{nm})$	$5 \pm 1.5$	$8 \pm 4.6$	$15 \pm 3.2$	$23 \pm 4.8$	$31 \pm 7.8$

$\text{CuFe}_2\text{O}_4/1 \text{ wt}\% \text{ CeO}_2$  nanocomposites. When the concentration of  $\text{CeO}_2$  increases above 5 wt%,  $\text{CeO}_2$  grows up on the  $\text{CuFe}_2\text{O}_4$  particles and modifies its surface, which is obvious from the SEM image. As well as the grain size of the materials decreases with the increasing concentration of  $\text{CeO}_2$  due to the hindering of grain growth [33]. This is the most important favorable property for delivering better electrochemical performance of the electrode materials [21–26].

The crystallinity, particle size and morphology of the as-prepared  $\text{CuFe}_2\text{O}_4/5 \text{ wt}\% \text{ CeO}_2$  nanocomposites were studied using TEM, HRTEM and SAED methods. The TEM image (Fig. 5a) shows that the particle size of the as-synthesized nanocomposite are in the range of 5–10 nm and the particles are found to be polydispersed materials. The HRTEM image (Fig. 5b) confirms the presence

of  $\text{CeO}_2$  phase and the ferrite material. The  $\text{CuFe}_2\text{O}_4$  spinel (2 2 0) planes with a  $d$  value of 2.92 Å and layered  $\text{CeO}_2$  (1 1 1) planes with a  $d$  value of 3.33 Å are observed, which confirm the composite nature of the as-prepared particles. SAED pattern (Fig. 5a(inset)) of  $\text{CuFe}_2\text{O}_4/\text{CeO}_2$  nanocomposites depicts well-defined rings for  $\text{CuFe}_2\text{O}_4$ . The presence of bright spots for  $\text{CeO}_2$  may be attributed to the composite and polycrystalline nature of the prepared materials.

### 3.3. Electrical properties

The frequency-dependent ac conductivity of the samples  $\text{CuFe}_2\text{O}_4/x\text{CeO}_2$  ( $x=0, 1, 5, 10$  and 20 wt%) measured at room temperature is shown in Fig. 6. It is well known that three different effects are involved in the ac conductivity, i.e., electrode effect, dc plateau, and defect processes [34]. It can be seen that two different regions are observed in the conductivity plot within the measured

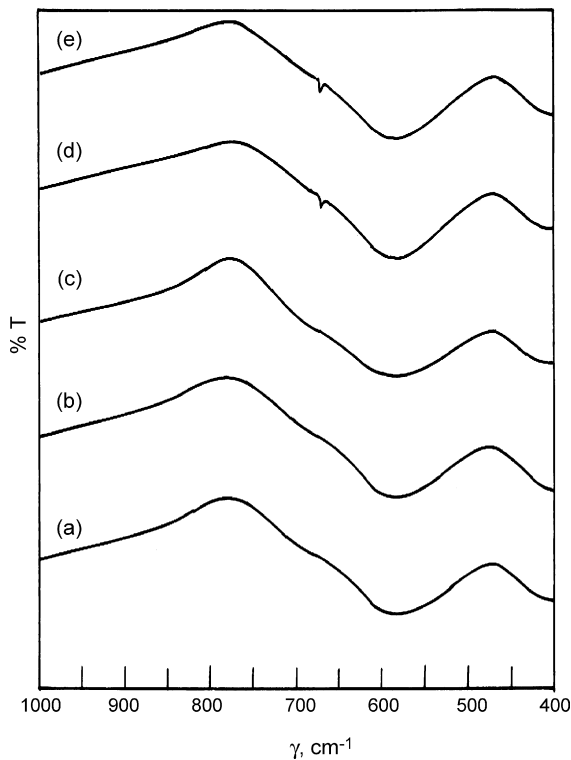


**Fig. 2.** FT-IR spectra of  $\text{CuFe}_2\text{O}_4/x \text{ wt}\% \text{ CeO}_2$  nanocomposites: (a)  $x=0$ , (b)  $x=1$ , (c)  $x=5$ , (d)  $x=10$  and (e)  $x=20$ .

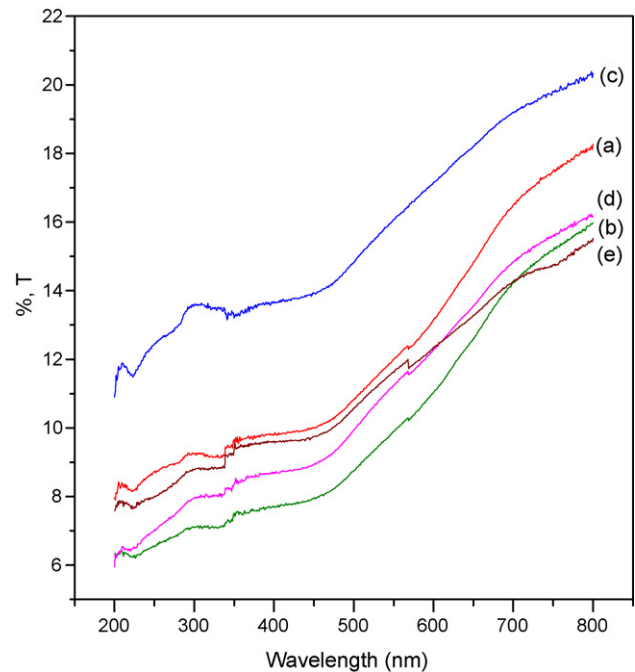


**Fig. 3.** UV-vis spectra of  $\text{CuFe}_2\text{O}_4/x \text{ wt}\% \text{ CeO}_2$  nanocomposites: (a)  $x=0$ , (b)  $x=1$ , (c)  $x=5$ , (d)  $x=10$  and (e)  $x=20$ .

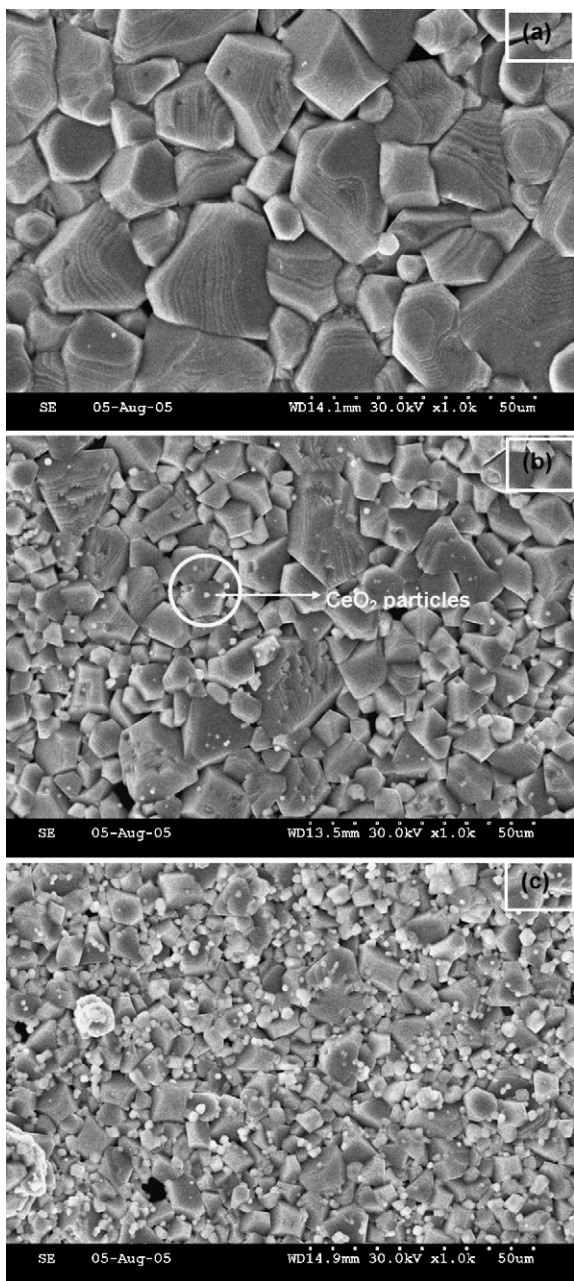


Fig. 4. SEM images of (a) CuFe<sub>2</sub>O<sub>4</sub>/1 wt% CeO<sub>2</sub>, (b) CuFe<sub>2</sub>O<sub>4</sub>/5 wt% CeO<sub>2</sub> and (c) CuFe<sub>2</sub>O<sub>4</sub>/20 wt% CeO<sub>2</sub> nanocomposites.

frequency window. One is low frequency plateau region and the other is high frequency dispersion region. At high frequency, all the curves are merged together indicating the formation of disordered solids. The plateau region shows the frequency-independent behaviour corresponding to the dc conductivity. The frequency dependent behaviour is observed at higher frequency which corresponds to ac conductivity and obeys the Joncher's Power law [35];  $\sigma_{\omega} = \sigma_{dc}(1 + (f/f_p)^n)$ , where  $n$  is the frequency exponent in the range of  $0 < n < 1$ ,  $\sigma_{dc}$  is the dc conductivity,  $f$  and  $f_p$  are applied frequency and relaxation frequency, respectively. According to the literature, an  $n$  value smaller than unity indicates the conduction through hopping mechanism and above one is due to localized hopping [36]. Below the relaxation frequency, the conductivity is constant and frequency independent. Above  $f_p$  the conduction mechanism is believed to be sub-diffusive and the conductivity is ac conductivity

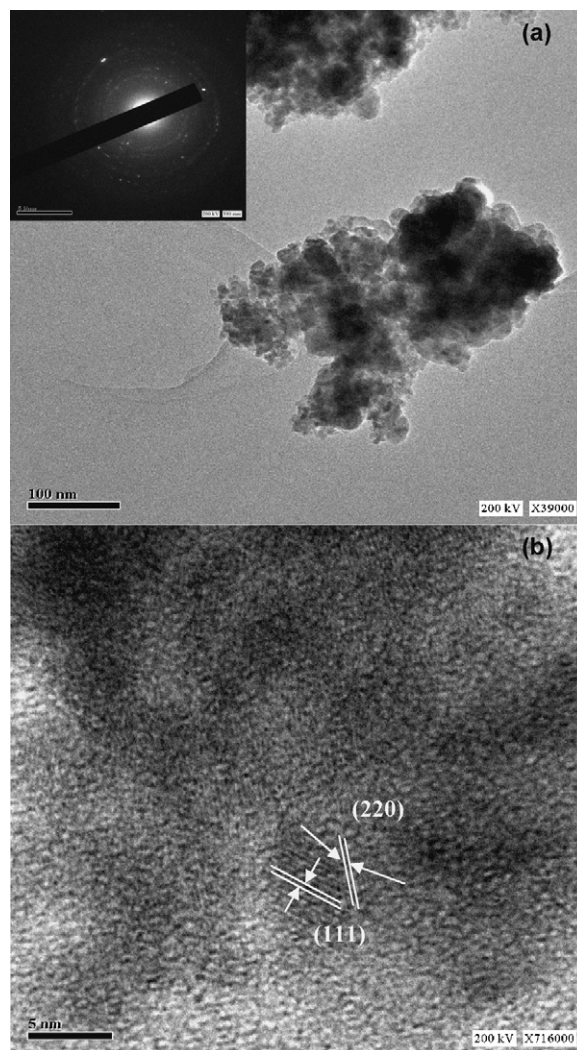


Fig. 5. TEM (a), HRTEM (b) and SAED ((a) inset) images of CuFe<sub>2</sub>O<sub>4</sub>/5 wt% CeO<sub>2</sub> nanocomposites.

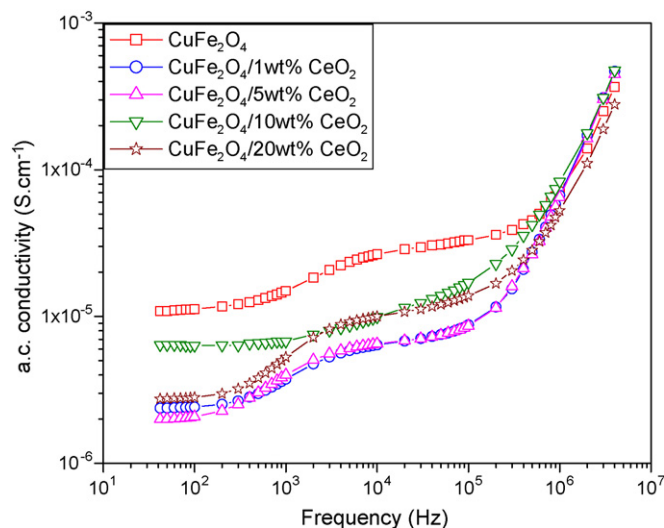


Fig. 6. ac electrical conductivity of CuFe<sub>2</sub>O<sub>4</sub>/x CeO<sub>2</sub> nanocomposites.

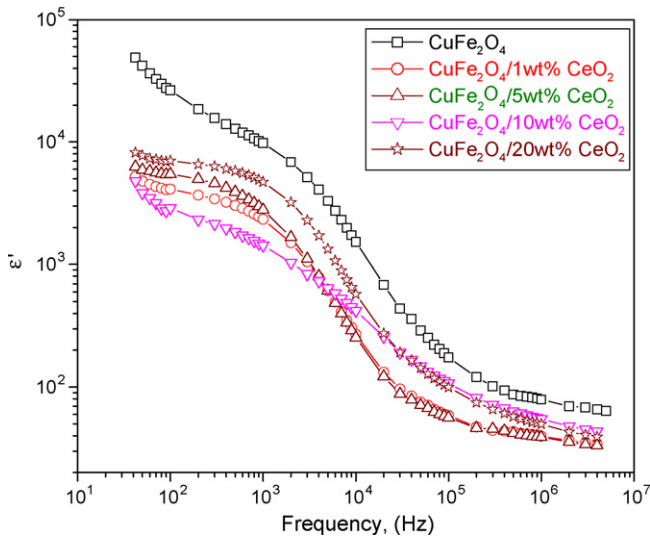


Fig. 7. Dielectric constant ( $\epsilon'$ ) vs. frequency of  $\text{CuFe}_2\text{O}_4/x \text{CeO}_2$  nanocomposites.

that depends on frequency. In this region, the transport is dominated by the contribution of hopping of infinite clusters. According to electron hopping model suggested by Heikes and Johnston [37], the conduction mechanism is the hopping of  $\text{Fe}^{2+}$  and  $\text{Fe}^{3+}$  ions as well as  $\text{Cu}^{2+}$  and  $\text{Cu}^{1+}$  in the adjacent octahedral sites in the spinel lattice. Fig. 6 also explains the effect of  $\text{CeO}_2$  addition on the frequency dependent ac conductivity of  $\text{CuFe}_2\text{O}_4$ . It can be observed that at low frequencies no significant improvement of the electrical conductivity of  $\text{CuFe}_2\text{O}_4$  could be observed while at higher frequencies the conductivity increases with the increasing addition of  $\text{CeO}_2$  up to 10 wt%. This may be explained by the fact that when an ion with variable valency enters the structure, charged vacancies are produced in order to maintain the local charge neutrality. Since  $\text{Cu}^{2+}$  ions are substituted by  $\text{Ce}^{4+}$  ions, negative ion vacancies or oxygen vacancies are created which result in high conductivity [38]. At higher concentration of  $\text{CeO}_2$  (>10 wt%), the conductivity values decrease due to the formation of large number of secondary phases, which hinders the electron hopping between the adjacent sites [33]. In general, the tetravalent ions act as the electrostatic trapping centres when they are substituted in the spinel matrix and thereby reduces the conductivity. Similar observations have also been reported for  $\text{Ti}^{4+}$  substituted  $\text{MgFe}_2\text{O}_4$  and  $\text{Ce}^{4+}$  substituted  $\text{NiAl}_2\text{O}_4$  [29,39].

The frequency dependent dielectric constant ( $\epsilon'$ ) of  $\text{CuFe}_2\text{O}_4/\text{CeO}_2$  nanocomposites measured at room temperature is shown in Fig. 7. It can be seen that  $\epsilon'$  decreases with increasing frequency and gets saturated at higher frequency. The decrease in dielectric constant with increasing frequency is due to the fact that the electronic exchange between the  $\text{Fe}^{2+}$  and  $\text{Fe}^{3+}$  ions cannot follow the externally applied frequency and will also obey the Debye relaxation process. On the other hand, the non-Debye behaviour is observed at high frequencies, which indicates the possible cation motion through the conduction pathways. It is seen that the values of dielectric constant decreases with increasing concentration of  $\text{CeO}_2$ . This variation mainly depends upon the number of space charge carriers and the resistivity of the samples, i.e., the increase in resistivity with the addition of  $\text{CeO}_2$ , prevents the flow of space charge carriers and therefore low value of dielectric constant is observed [40].

Fig. 8 shows the variation of loss tangent with frequency for all the samples measured at room temperature. At low frequency the loss tangent is very high because the energy required for the elec-

tronic exchange between  $\text{Fe}^{2+} \rightleftharpoons \text{Fe}^{3+}$  is large and it decreases with increasing frequency. At higher frequencies, lower energy is enough to maintain the charge and hence the loss tangent is low. The mechanism can be correlated with the Koops bi-layer formation. At lower frequency, the grain boundary effect is predominant and so the resistivity of the materials is high while at high frequency, the maximum conductivity is observed due to the larger grain effect. Fig. 8 also explains the effect of  $\text{CeO}_2$  on the loss tangent values of copper ferrite. At low frequency the loss tangent values increase with increasing concentration of  $\text{CeO}_2$  and at high frequency, the values are low compared to the pristine copper ferrite. The dielectric relaxation peaks are observed at 30 kHz for  $\text{CuFe}_2\text{O}_4$  and 20 kHz for 1, 5 and 20 wt%  $\text{CeO}_2$  composites. This happens when the jumping frequency of the localized charge carriers are approximately equal to the externally applied frequency. The appearance of dielectric relaxation peaks could be related to the collective contribution of both the type of charge carriers, which could be explained by Rezlescu model [41]. For  $\text{CuFe}_2\text{O}_4/10 \text{wt}\% \text{CeO}_2$  composite, no peak is observed in the measured frequency window. However, it seems that the peak may have fall below the frequency range of 20 kHz. Similar types of observations have already been reported for  $\text{Ti}^{4+}$  substituted Li-ferrite and Zn substituted Li- $\text{MgFe}_2\text{O}_4$  [42,43]. The observed shifting of relaxation frequency compared with the parent  $\text{CuFe}_2\text{O}_4$  is due to the decreasing concentration of  $\text{Fe}^{2+}$  ions in the octahedral sites, which is responsible for the polarization process due to the addition of foreign ions [44]. Even though, at lower frequencies the 10 wt%  $\text{CeO}_2$  sample shows the largest loss tangent values, which is due to its conductivity.

### 3.4. Magnetic properties

The Mössbauer spectra of  $\text{CuFe}_2\text{O}_4/x\text{CeO}_2$  ( $x = 0, 1, 5, 10, 20 \text{wt}\%$ ) samples measured at room temperature are shown in Fig. 9. The strategy for fitting the Mössbauer spectra was based on the fact that owing to the supertransfer mechanism in spinel ferrites [45,46], the  $\text{Fe}^{3+}[\text{B}]$  ion experiences local fields that reflect the distribution of magnetic ions in its neighbourhood, i.e., the  $\text{Fe}^{3+}[\text{B}]$  ion is very sensitive to the number of its (A)-site nearest magnetic neighbours. This results in a broad distribution of the [B]-site magnetic hyperfine fields ([B]-site subspectrum displays a broadening). Thus, the subspectra belonging to octahedrally coordinated iron cations

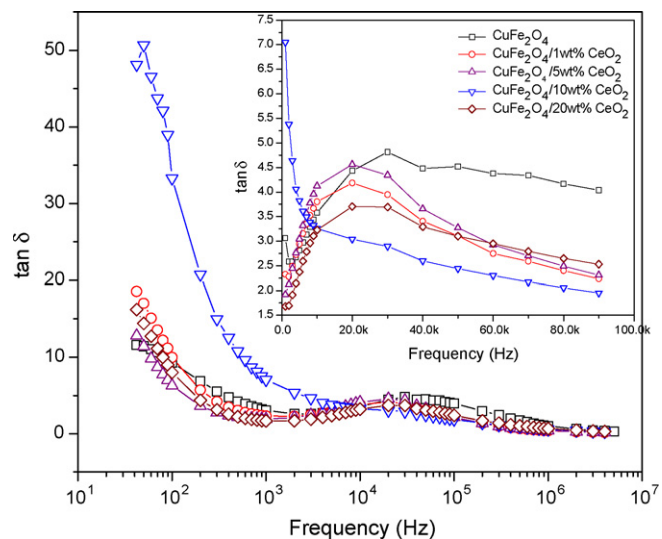


Fig. 8. Dielectric loss tangent vs. frequency of  $\text{CuFe}_2\text{O}_4/x \text{CeO}_2$  nanocomposites, (Inset shows the relaxation frequency of the composites).

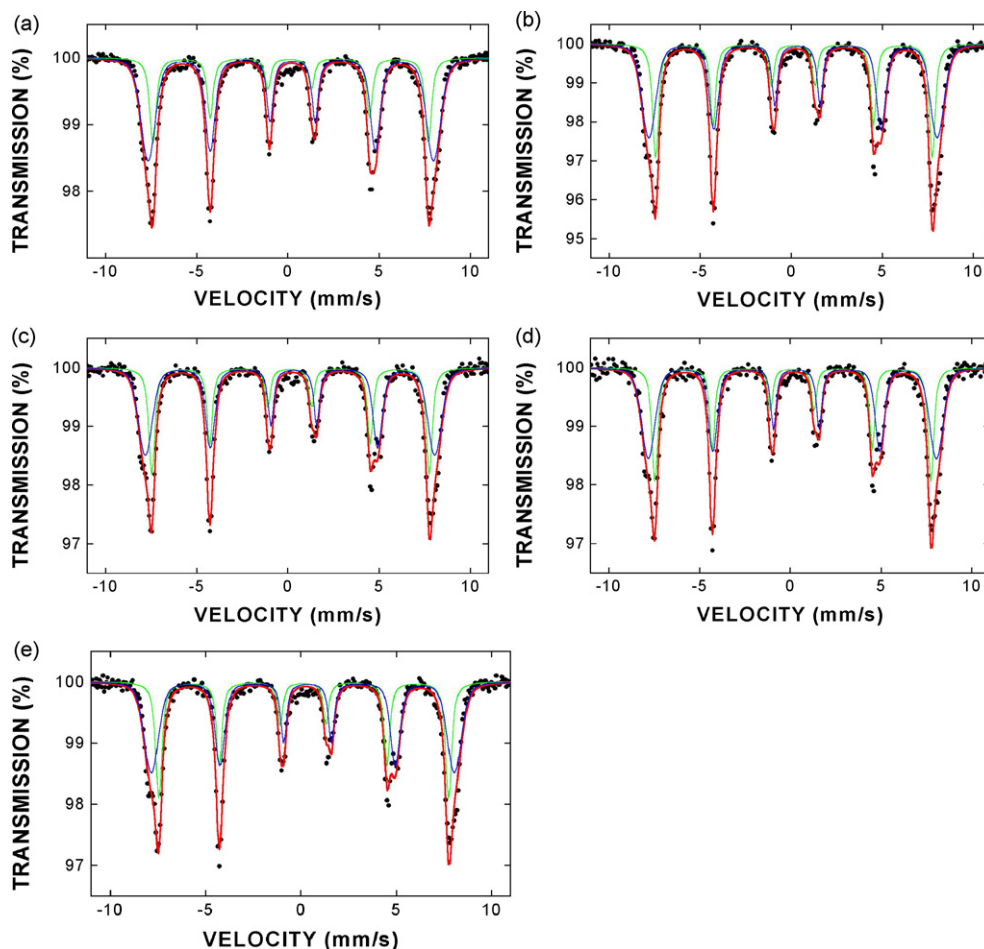


Fig. 9. Mössbauer spectra of  $\text{CuFe}_2\text{O}_4/x$  wt%  $\text{CeO}_2$  nanocomposites:  $x=0$  (a),  $x=1$  (b),  $x=5$  (c),  $x=10$  (d) and  $x=20$  (e).

were fitted with a broad field distribution characterized by Gaussian width of the magnetic field component  $\sigma \sim 1.9$  T. On the other hand, local magnetic fields experienced by  $\text{Fe}^{3+}$ (A) are independent of the detailed distribution of magnetic [B]-site nearest neighbours [47–49]. Thus, the (A)-site lines were fitted with a narrow field distribution characterized by Gaussian width of about 0.4 T. The spectra of all the samples show two well-defined sextets belonging to the tetrahedral and octahedral sites of  $\text{Fe}^{3+}$  ions, which confirm that the synthesized materials possess inverse spinel structure. The sextet with the lower isomer shift and hyperfine field values corresponds to the tetrahedral sites and the higher isomer shift and hyperfine field values exhibit the octahedral sites. The measured values of isomer shift (IS), quadrupole splitting (QS), magnetic hyperfine field ( $B$ ), Lorentzian line width ( $\Gamma$ ), relative intensity ( $I$ ) and degree of inversion ( $\lambda$ ) are given in Table 3.

It is well known that the isomer shift of  $\text{Fe}^{2+}$  and  $\text{Fe}^{3+}$  ions lies within a range of  $0.6\text{--}1.7$   $\text{mm s}^{-1}$  and  $0.1\text{--}0.5$   $\text{mm s}^{-1}$ , respectively. The isomer shift values given in Table 3 enumerate that the iron ions in  $\text{CuFe}_2\text{O}_4/x\text{CeO}_2$  ( $x=0, 1, 5, 10, 20$  wt%) samples are present only in the  $\text{Fe}^{3+}$  state. Due to  $\text{Ce}^{4+}$  substitution interestingly, no change in the oxidation state of iron ions is observed in all the samples. There is no systematic change in the isomer shift values of all the systems, which implies that the s-electron density is not much altered with the  $\text{CeO}_2$  addition. The values of quadrupole splitting of the composites are negligibly small, which is attributed to the overall symmetry of the  $\text{Fe}^{3+}$  surroundings, which is maintained with the addition of  $\text{CeO}_2$ . Compared with all the nanocomposites, the parent  $\text{CuFe}_2\text{O}_4$  exhibited a slightly enhanced value of QS, which indicates an altered distribution of ionic charges in the sub-lattices [50].

Table 3

Mössbauer parameters of the  $\text{CuFe}_2\text{O}_4/x\text{CeO}_2$  ( $x=0, 1, 5, 10, 20$  wt%) samples measured at room temperature

Compounds	Mössbauer parameters									
	$IS_{(A)}$ ( $\text{mm s}^{-1}$ )	$IS_{[B]}$ ( $\text{mm s}^{-1}$ )	$QS_{(A)}$ ( $\text{mm s}^{-1}$ )	$QS_{[B]}$ ( $\text{mm s}^{-1}$ )	$B_{(A)}$ (T)	$B_{[B]}$ (T)	$\Gamma$ ( $\text{mm s}^{-1}$ )	$I_{(A)}$ (%)	$I_{[B]}$ (%)	$\lambda$
$\text{CuFe}_2\text{O}_4$	0.1396 (67)	0.2227 (50)	0.0213 (65)	−0.0525 (49)	46.830 (43)	48.517 (78)	0.1828 (54)	31.3 (17)	68.7 (17)	0.626
$\text{CuFe}_2\text{O}_4/1$ wt% $\text{CeO}_2$	0.1462 (39)	0.2340 (47)	0.0193 (43)	−0.1191 (50)	47.140 (28)	49.19 (11)	0.1682 (44)	39.1 (11)	60.9 (11)	0.782
$\text{CuFe}_2\text{O}_4/5$ wt% $\text{CeO}_2$	0.1395 (64)	0.2338 (76)	0.0170 (67)	−0.1067 (78)	47.171 (45)	49.19 (11)	0.1668 (70)	39.1 (18)	60.9 (18)	0.782
$\text{CuFe}_2\text{O}_4/10$ wt% $\text{CeO}_2$	0.1414 (66)	0.2341 (82)	0.0181 (69)	−0.1093 (85)	47.131 (47)	49.19 (11)	0.1592 (74)	39.2 (19)	60.8 (19)	0.784
$\text{CuFe}_2\text{O}_4/20$ wt% $\text{CeO}_2$	0.1416 (47)	0.2345 (60)	0.0171 (50)	−0.1227 (62)	47.118 (34)	49.266 (81)	0.1635 (53)	40.1 (13)	59.9 (13)	0.802

IS: the average isomer shift; QS: the average quadrupole splitting;  $B$ : the average magnetic hyperfine field;  $\Gamma$ : Lorentzian line half-width;  $I$ : relative intensity;  $\lambda$ : the degree of inversion.

The hyperfine field values of (A)-sites are slightly increased with increasing concentration of CeO<sub>2</sub>, but no remarkable change is observed for [B]-site hyperfine magnetic fields. The average values of the hyperfine magnetic fields experienced by iron ions in the two sub-lattices are about 47.1 and 49.2 T, respectively, for all the CuFe<sub>2</sub>O<sub>4</sub>/CeO<sub>2</sub> composites. These values are characteristic for ferric (Fe<sup>3+</sup>) ions in tetrahedral and octahedral sub-lattices of CuFe<sub>2</sub>O<sub>4</sub> spinel [51]. The values of the degree of inversion (Table 3) clearly indicate that the addition of CeO<sub>2</sub> caused the migration of some of the iron ions from [B]-site to (A)-site.

#### 4. Conclusions

This is an ever first attempt to synthesize CuFe<sub>2</sub>O<sub>4</sub>/CeO<sub>2</sub> nanocomposites by simple combustion method. XRD analysis confirms that the synthesized CuFe<sub>2</sub>O<sub>4</sub>/CeO<sub>2</sub> materials have the tetragonal structure and the composite behaviour. FT-IR spectra reveal the stretching vibration of the Fe–O and Ce–O bonds. The observed optical band gap values confirmed that the synthesized materials exhibit semiconducting behaviour. The nanocomposite nature of the materials has been evidenced by SEM, TEM, and HRTEM images. The particle size of CuFe<sub>2</sub>O<sub>4</sub>/CeO<sub>2</sub> nanocomposites decreases with increasing concentration of CeO<sub>2</sub>. The ac and dielectric constant values decrease with increasing concentration of CeO<sub>2</sub>. Mössbauer spectra confirm the +3 valency of the present iron ions in the structure as well as the inverse spinel structure of the prepared materials.

#### Acknowledgements

The authors express their gratitude to Prof. A.K. Shukla, Director, CECRI, Karaikudi, India for his keen interest in this work. The authors are very much grateful to Prof. S. Selvasekarapandian (Bharathiar University, Coimbatore) for extending the facility of ac conductivity studies.

#### References

- [1] J. Wang, J.J. Luo, Q. Fan, M. Suzuki, I.S. Suzuki, M.H. Engelhard, Y. Lin, N. Kim, J.Q. Wang, C.J. Zhong, *J. Phys. Chem. B* 109 (2005) 21593.
- [2] M.V. Vasic, B. Antic, A. Kremenovic, A.S. Nikolic, M. Stoiljkovic, N. Bibic, V. Spasojevic, P.H. Colomban, *Nanotechnology* 17 (2006) 4877.
- [3] N. Murillo, E. Ochoteco, Y. Alesanco, J.A. Pomposo, J. Rodriguez, J. Gonzalez, J.J.D. Val, J.M. Gonzalez, M.R. Brtel, F.M.V. Feria, A.R.A. Lopez, *Nanotechnology* 15 (2004) S322.
- [4] W. Shi, H. Zeng, Y. Sahoo, T.Y. Ohulchansky, Y. Ding, Z.L. Wang, M. Swihart, P.N. Prasad, *Nanoletters* 6 (2006) 875.
- [5] X. Lu, G. Liang, Y. Zhang, W. Zhang, *Nanotechnology* 18 (2007) 015701.
- [6] M. Arruebo, R.F. Pacheco, S. Irusta, J. Arbiol, M. Ibarra, J. Santamaría, *Nanotechnology* 151 (2006) 4057.
- [7] Y.Q. Chu, Z.W. Fu, Q.Z. Qin, *Electrochim. Acta* 49 (2004) 4915.
- [8] X. Yang, X. Wang, Z. Zhang, *J. Cryst. Growth* 277 (2005) 463.
- [9] R. Alcántara, M. Jaraba, P. Lavela, J.L. Tirado, J.C. Jumas, J.O. Fourcade, *Electrochim. Commun.* 5 (2003) 16.
- [10] Y.N. NuLi, Q.Z. Qin, *J. Power Sources* 142 (2005) 292.
- [11] Y.N. NuLi, Y.Q. Chu, Q.Z. Qin, *J. Electrochem. Soc.* 151 (2004) A1077.
- [12] N. Sharma, K.M. Shaju, G.V. Subba Rao, B.V.R. Chowdari, *J. Power Sources* 124 (2003) 204.
- [13] R.K. Selvan, N. Kalaiselvi, C.O. Augustin, C.H. Doh, C. Sanjeeviraja, *J. Power Sources* 157 (2006) 522.
- [14] V. Krishnan, R.K. Selvan, C.O. Augustin, A. Gedankan, H. Bertagnolli, *J. Phys. Chem. C* 111 (2007) 16724.
- [15] F. Zhou, X. Ni, Y. Zhang, H. Zheng, *J. Colloid Interf. Sci.* 307 (2007) 135.
- [16] F. Zhou, X. Zhao, H. Xu, C. Yuan, *J. Phys. Chem. C* 111 (2007) 1651.
- [17] L. Yuan, Z.P. Guo, K. Konstantinov, H.K. Liu, S.X. Dou, *J. Power Sources* 159 (2006) 345.
- [18] S.J. Bao, Q.L. Bao, C.M. Li, Z.L. Dong, *Electrochim. Commun.* 5 (2007) 1233.
- [19] S. Kanzaki, A. Yamada, R. Kanno, *J. Power Sources* 165 (2007) 403.
- [20] S.A. Needham, G.X. Wang, H.K. Liu, *J. Power Sources* 159 (2006) 254.
- [21] S.T. Myung, K. Izumi, S. Komaba, H. Yashiro, H.J. Bang, Y.K. Sun, N. Kumagai, *J. Phys. Chem. C* 111 (2007) 4061.
- [22] Z. Zhang, Z. Gong, Y. Yang, *J. Phys. Chem. B* 108 (2004) 17546.
- [23] H. Miyashiro, Y. Kobayashi, S. Seki, Y. Mita, A. Usami, M. Nakayama, M. Wakihara, *Chem. Mater.* 17 (2005) 5603.
- [24] H.W. Ha, N.J. Yun, K. Kim, *Electrochim. Acta* 52 (2007) 3236.
- [25] H.W. Ha, N.J. Yun, M.H. Kim, M.H. Woo, K. Kim, *Electrochim. Acta* 51 (2006) 3297.
- [26] H.W. Ha, K.H. Jeong, N.J. Yun, M.Z. Hong, K. Kim, *Electrochim. Acta* 50 (2005) 3764.
- [27] R.K. Selvan, C.O. Augustin, C. Sanjeeviraja, V.G. Pol, A. Gedanken, *Mater. Chem. Phys.* 99 (2006) 109.
- [28] K. Lagarec, D.G. Rancourt, RECOIL, Mössbauer Spectral Analysis Software for Windows, Version 1.02, Department of Physics, University of Ottawa, Ottawa, 1998.
- [29] C.O. Augustin, K. Hema, L.J. Berchmans, R.K. Selvan, R. Saraswathi, *Phys. Stat. Sol. A* 202 (2005) 1017.
- [30] A. Soldatov, T.S. Ivanchenko, S.D. Longa, A. Kotani, Y. Iwamoto, A. Bianconi, *Phys. Rev. B* 50 (1994) 5074.
- [31] A. Bumajdad, M.I. Zaki, J. Eastoe, L. Pasupulety, *Langmuir* 20 (2004) 11223.
- [32] S.M. Chang, R.A. Doong, *J. Phys. Chem. B* 108 (2004) 18098.
- [33] N. Rezlescu, C. Pasnicu, M.L. Craus, *J. Phys. Cond. Matter* 6 (1994) 5707.
- [34] R. James, C. Prakash, G. Prasad, *J. Phys. D: Appl. Phys.* 39 (2006) 1635.
- [35] A.K. Joncher, *Nature* 267 (1977) 673.
- [36] M. Vijayakumar, S. Selvasekarapandian, M.S. Bhuvaneshwari, G. Hirankumar, G. Ramaprasad, R. Subramanian, P.C. Angelo, *Physica B* 334 (2003) 390.
- [37] R.R. Heikes, W.D. Johnston, *J. Chem. Phys.* 26 (1957) 582.
- [38] S. Balaji, R.K. Selvan, L.J. Berchmans, S. Angappan, K. Subramanian, C.O. Augustin, *Mater. Sci. Eng. B* 119 (2005) 119.
- [39] F.A. Radwan, M.A. Ahmed, G. Addelatif, *J. Phys. Chem. Solids* 64 (2001) 2465.
- [40] A. Lakshman, P.S.V. Subba Rao, B. Parvathes Rao, K.H. Rao, *J. Phys. D: Appl. Phys.* 38 (2005) 673.
- [41] N. Rezlescu, E. Rezlescu, *Phys. Stat. Sol. A* 23 (1974) 575.
- [42] M.B. Reddy, P.V. Reddy, *J. Phys. D: Appl. Phys.* 24 (1991) 975.
- [43] A.M. Shaikh, S.S. Bellad, B.K. Chougule, *J. Magn. Magn. Mater.* 195 (1999) 384.
- [44] P. Muralidharan, V. Venkateswaralu, N. Satyanarayana, *Solid State Ionics* 166 (2004) 27.
- [45] G.A. Sawatzky, F.V.D. Woude, A.H. Morrish, *Phys. Rev.* 187 (1969) 747.
- [46] R.E. Vandenberghe, E. De Grave, in: G.J. Long, F. Grandjean (Eds.), *Mössbauer Spectroscopy Applied to Inorganic Chemistry*, vol. 3, Plenum Press, NY, 1989, p. 59.
- [47] G.A. Sawatzky, F.V.D. Woude, A.H. Morrish, *Phys. Rev.* 183 (1969) 383.
- [48] F.V.D. Woude, G.A. Sawatzky, *Phys. Rev. B* 4 (1971) 3159.
- [49] V. Sepelak, D. Baabe, F.J. Litterst, K.D. Becker, *J. Appl. Phys.* 88 (2000) 5884.
- [50] A. Lakshman, P.S.V. Subba Rao, K.H. Rao, *Mater. Lett.* 60 (2006) 7.
- [51] B.J. Evans, S. Hafner, *J. Phys. Chem. Solids* 29 (1968) 1573.